Kinematic properties of regions that can involve persistent contrails

Sina Maria Hofer[1] and Klaus Martin Gierens[1]

[1]Deutsches Zentrum für Luft- und Raumfahrt, Institut für Physik der Atmosphäre, Oberpfaffenhofen, Germany

Correspondence: Sina Maria Hofer (sina.hofer@dlr.de)

Abstract.

Contrails can last for many hours in the sky if they form in so-called ice supersaturated regions (ISSRs). Contrail formation is possible once the ambient air is sufficiently moist and cold (below $-40\,°C$) such that the water vapour in the exhaust of an aircraft engine transiently becomes water saturated, which initiates formation of droplets which immediately freeze. Contrails are persistent when the ambient relative humidity with respect to ice is at least $100\,\%$. Cirrus clouds and contrails consist of material ice crystals, which move with the wind. Ice supersaturation is an immaterial feature, which does not generally move with the wind. However, the exact movement of ice supersaturated regions and how they move in comparison to the winds, is currently unknown. We analyse their relation using data for aviation weather forecasts, the so called WAWFOR package, from the German Weather Service (DWD). Our results demonstrate the general kinematic differences and similarities of the movement of ISSRs in comparison to the motion of the air in and through the ISSRs. We show that the ISSRs on average move slower than the wind at the same location, the direction of movement is usually quite similar and the distributions of both velocities follow Weibull distributions. The almost identical direction of the movements is beneficial for contrail lifetimes, but the lifetime of contrails is not generally determined by the lifetime of ISSRs. It happens that contrails are blown out of ISSRs with the wind. We assume that our study can be used as a basis and starting point for further analyses and descriptions of the movement of ISSRs and their movement properties. Furthermore, our method of analysis is applicable to other extended features or areas, for instance for areas where aircraft non-CO_2 emissions would have a particularly large climate effect.

1 Introduction

Climate change is ongoing and the necessity to take actions against it is getting more and more pressing. All sectors have to reduce their share of the overall climate warming, including aviation. Although the latter sector contributes currently only about 3.5% to the radiative forcing of climate, it cannot be exempted from urgent measures because aviation demand increases at a more rapid pace than the fuel need for a unit distance (the specific fuel consumption) gets reduced by commissioning of more efficient engines (Grewe et al., 2021; Lee et al., 2021). A peculiarity of aviation is its relatively strong climate impact induced by non-CO_2 emissions and effects. The individual non-CO_2 effects from a single flight depend strongly on the actual ambient conditions (synoptic weather situation, ambient cloudiness, position of the sun, etc.) which may open a possibility for climate- and environmentally friendly air transport by explicitly searching for routes where the climate impact is minimal (Matthes et al., 2021; Yin et al., 2023). An important part of climate-aware aviation is the avoidance of those persistent contrails

that contribute to the warming of climate. Persistent contrails can form if a thermodynamic condition, the so-called Schmidt-Appleman criterion, introduced by Schumann (1996), is fulfilled and when the flights transect a so-called ice supersaturated region (ISSR, see Gierens et al., 2012, for a review), where the relative humidity with respect to ice $RH_i \geq 100\%$.

30   The Schmidt-Appleman criterion is often fulfilled once the ambient temperature is a few degrees below $-40°$C. Supersaturation with respect to ice or in short ice supersaturation (ISS) occurs in particularly cold and humid regions in the troposphere and it is primarily found in areas below the tropopause (Spichtinger et al., 2003; Petzold et al., 2020). Both conditions, low temperature and ice supersaturation, are found in regions that are termed cold ice supersaturated regions (CISSRs) by Irvine and Shine (2015). Ice supersaturated regions (ISSRs) arise mainly from large-scale vertical movements where rising air masses

35   containing water vapour cool adiabatically and the relative humidity increases (Gierens and Brinkop, 2012). CISSRs and ISSRs are mostly the same areas since the Schmidt-Appleman criterion is most often fulfilled in ISSRs. ISS is often connected to slightly stable to neutral stratification because of the increases in the temperature gradient of rising air layers (Gierens et al., 2022).

    ISSRs become visible when either natural cirrus clouds form, or when aircraft fly through them because contrails that form

40   in ISSRs are persistent and can remain in the sky for up to several hours. In spite of this close relation, contrails and their ambient ISSRs do not generally have the same lifetime (Bakan et al., 1994). While cirrus and contrails consist of material ice crystals which move with the wind, ISS is an immaterial feature which does not generally move with the wind. Individual contrails and cirrus clouds may be driven out of the parental ISSR, which sooner or later terminates their existence when the ice crystals get into subsaturated air and sublimate. That is, contrails and cirrus on one side and ISSRs on the other have different

45   lifetimes. The lifetime of ISSRs themselves is limited by the dynamics of the atmosphere. As soon as downdraft and thus adiabatic warming occurs, the ice supersaturation decreases and disappears eventually. The different lifetimes motivated us to study the differences between the real wind and the motion (pseudo-wind) of ISSRs, or more precisely, CISSRs. A peculiar difference is that ISSRs have an initiation and an end in time, which also marks the end of their motion. In contrast, the wind is ceaseless (c.f. the apt title of an old textbook, "The ceaseless wind" by Dutton (1986)).

50   For this initial study and the sake of simplicity, we consider horizontal motions only. We use data from a weather forecast model to compare the motion of the air to the movement of CISSRs, that is, we compare the wind with a kind of pseudo-wind. The paper is organised as follows: First we describe our data source in section 2. Methods of the data analysis are compiled in section 3. Result are presented in section 4 and these are discussed in section 5. At the end we conclude in section 6.

2 Data

55 The German Weather Service (DWD) provides aviation weather forecasts four times per day (WAWFOR data), based on the weather forecast model ICON (Zängl et al., 2015), with hourly temporal resolution. The usual WAWFOR data inform aviation users on temperature, humidity, winds, etc. (WAWFOR Package 1), but for the German D-KULT project (Demonstrator Klima- und Umweltfreundlicher Lufttransport; Demonstration of climate- and environmentally friendly air transport), additional datasets are produced that inform on the potential to form persistent contrails, i.e. on CISSRs, and on the climate effect

60 of other gaseous emissions from aviation. The additional information that is used here is in particular

PPC: potential of persistent contrails — a binary value $(0/1)$;

PPC_{prob}: fraction of ensemble forecast members that have $PPC = 1$ — a real number between 0 and 1.

PPC is computed from the Schmidt-Appleman criterion (SAC) (Schumann, 1996) applying an overall propulsion efficiency of $\eta = 0.365$ and using temperature and relative humidity from the regular forecast. In order to compensate a low humidity

65 bias in the forecast (Gierens et al., 2022), situations with values of relative humidity with respect to ice (RH_i) in excess of 93% are considered ice (super) -saturated (Hofer et al., 2024). PPC_{prob} is simply the number of members of the 40-member forecast ensemble that predict $PPC = 1$, divided by the total number of ensemble members (40); It can thus obtain values $n/40; n \in \mathbb{N}_0, 0 \leq n \leq 40$. The meteorological data, PPC and PPC_{prob}, are available globally and with higher spatial resolution for the European region (EU nest, $0.0625° \times 0.0625°$, approx. $6.5\,\mathrm{km} \times 6.5\,\mathrm{km}$). The latter are used here in an area from

70 $23.5°$W to $62.5°$E and $29.5°$N to $70.5°$N. Altitudes that are most relevant for air traffic, between 8 and $12\,\mathrm{km}$ and with $0.5\,\mathrm{km}$ increments, are used. They correspond approximately to pressures $p \in (197, 207, 227, 238, 262, 287, 301, 329, 360)\,\mathrm{hPa}$.

$PPC = 1$ thus marks CISSR grid points where persistent contrails are possible, and $PPC = 0$ marks all the rest where either no contrails at all or merely short contrails can be formed. Note that CISSRs and ISSRs are mostly the same areas since the Schmidt-Appleman criterion is most often fulfilled in ISSRs. Only a few percent of ISSRs are not cold enough for contrail

75 formation, but once a contrail is formed in a CISSR it can later spread into a slightly warmer ISSR (Wolf et al., 2023). Thus, we often write simply ISSR instead of CISSR. In addition, we use the wind data to compare it with the pseudo-velocity of ISSRs. The wind is given with its components in zonal (x) and meridional (y) directions.

The data covers April and May 2024. Due to missing data, 3 days have been excluded: April 30, May 14 and 28. We use data for each day at the time of analysis 12 UTC $+t$ hours, where $t \in (10, 11, ..., 20)\,\mathrm{h}$. As we will see later, we always examine

80 ISSRs that appear in three subsequent output times of a forecast run. The dataset contains 29595 of these groups of ISSRs.

3 Methods

3.1 Identification of ISSR pairs

In order to determine the kinematics of ISSRs we consider PPC and PPC_{prob} in subsequent hourly outputs of the WAWFOR data. A pseudo-velocity of these regions is determined numerically in a way analogously to the numerical determination of a

85 wind speed at a certain time. To determine the pseudo-velocity, $V_{\mathrm{ISSR}}(t_n)$, at a certain point in time, t_n (e.g. at time step n), the positions of the ISSR on the same pressure level at two additional times are needed, say at t_{n-1} and t_{n+1}. It is thus necessary to identify ISSRs at these three points in time in respective three outputs of the forecast. This task is solved first.

To identify ISSRs in several subsequent forecast steps, first their size (N, number of simply connected grid points, in longitude, latitude, and diagonally with $PPC = 1$) is determined. ISSRs consisting of less than 500 grid points are not considered

90 further. We introduced the limit of 500 ($N \geq 500$) to avoid examining small ISSR patches and to neglect this kind of noise. For all other ISSRs we calculate an analogue of a centre of mass, here termed centre of probability (COP) in the following way:

$$x_{\mathrm{COP}} = \frac{\sum_{n=1}^{N} PPC_{\mathrm{prob}_n} \cdot x_n}{\sum_{n=1}^{N} PPC_{\mathrm{prob}_n}} \qquad \text{and} \qquad y_{\mathrm{COP}} = \frac{\sum_{n=1}^{N} PPC_{\mathrm{prob}_n} \cdot y_n}{\sum_{n=1}^{N} PPC_{\mathrm{prob}_n}}. \tag{1}$$

Thus, each ISSR has one centre of probability in each forecast and pressure level. Note that $PPC_i = 1$ for all points that belong to a distinct ISSR, while outside it is zero (PPC_{prob} can be non-zero, even if $PPC = 0$; the sums do not extend over such points).

With the centres of probability at hand, Euclidean distances, $d_{i,j}$, of any pairs of COPs can be determined. ISSRs i, j are not identified if their distance exceeds $280\,\mathrm{km}$. However, for $d_{i,j} < 280\,\mathrm{km}$, we retain for each ISSR, respectively, the three candidate partners with the smallest distances. We assume $280\,\mathrm{km}$ as the maximum distance an ISSR can move within one hour since the maximum wind speed in the data is $282\,\mathrm{km\,h^{-1}}$.

A pair of ISSRs in a respective pair of forecasts must not change size N by more than 45%. From the three candidates, if they fulfil this condition, the partner with the smallest $d_{i,j}$ is selected. That is, a certain ISSR in one forecast hour is recognised in the adjacent forecast hour (previous or next).

It may happen that more than one ISSR at time t_n has the same partner at time t_{n-1}. In this case we find a unique recognition via a measure of similarity provided by the Hu-moments, in that we identify the pair having the smallest similarity difference (see Appendix A for more explanation). The other pair or pairs are not considered for the investigation. The same tests are performed between t_{n+1} and t_n and only if an ISSR is recognised in all three forecasts, its kinematics can be determined. This is described next.

3.2 Kinematics of ISSRs

To describe the dynamic motion of an ISSR, one needs to determine how fast it moves. This can be done in many ways, but the simplest way is chosen here, that is, the pseudo-velocity of an ISSR at t_n is taken as the Euclidean distance of its COP at t_{n+1} and t_{n-1} divided by the temporal difference:

$$V_{\mathrm{ISSR}_i}(t_n) \;=\; \frac{d(i, n+1, n-1)}{t_{n+1} - t_{n-1}}, \qquad \text{where} \tag{2}$$

$$d(i, n+1, n-1) \;=\; \sqrt{[x_{\mathrm{COP}_i}(t_{n+1}) - x_{\mathrm{COP}_i}(t_{n-1})]^2 + [y_{\mathrm{COP}_i}(t_{n+1}) - y_{\mathrm{COP}_i}(t_{n-1})]^2}. \tag{3}$$

$V_{\mathrm{ISSR}_i}(t_n)$ is the pseudo-velocity of ISSR i at time t_n, $d(i, n+1, n-1)$ is the Euclidean distance of the COPs of ISSR i at the two time steps before and after t_n. In our case, the coordinates are given as longitude and latitude. The conversion of distances on a great circle to distances in km is given in Appendix B.

In order to determine the direction of movement of an ISSR at t_n, the vector from its COP at t_{n-1} to the COP at t_{n+1} is used and its direction is taken for the direction of the movement of the ISSR. This yields the Cartesian components u_{ISSR} and v_{ISSR} of an ISSR.

3.3 Characterisation of the winds

As mentioned before, the velocity of the movement of the ISSRs and the wind speed are different. Since the wind and its Cartesian components u_wind and v_wind are only predicted for the grid points, the grid point that is closest to the centre of probability of an ISSR is selected. The magnitude of the wind speed is calculated using the components as follows:

$$V_\mathrm{wind} = \sqrt{u_\mathrm{wind}^2 + v_\mathrm{wind}^2}. \tag{4}$$

3.4 Angle between the motion of the ISSRs and the winds

The angle, δ, between the direction of motion of the ISSR and the direction of the local wind is the angle between the two vectors $\boldsymbol{V}_\mathrm{ISSR}$ and $\boldsymbol{V}_\mathrm{wind}$ with the following convention: If it needs a anticlockwise rotation to turn from $\boldsymbol{V}_\mathrm{ISSR}$ to $\boldsymbol{V}_\mathrm{wind}$, the angle $\delta > 0$, otherwise $\delta \leq 0$. δ ranges from $-180°$ to $180°$ (or $-\pi \leq \delta \leq \pi$ in radians). In order to retain the sign in this convention, we use the triple product, $\langle \cdot, \cdot, \cdot \rangle$, with the three unit vectors $\hat{\boldsymbol{V}}_\mathrm{ISSR}$, $\hat{\boldsymbol{V}}_\mathrm{wind}$, and $\hat{\boldsymbol{z}}$. The latter points upward into the vertical direction. A preliminary result is

$$\delta' = \arcsin\left(\langle \hat{\boldsymbol{V}}_\mathrm{ISSR}, \hat{\boldsymbol{V}}_\mathrm{wind}, \hat{\boldsymbol{z}} \rangle\right). \tag{5}$$

The result is not yet unique, because the $\sin$ function is not unique in the range $[-\pi, \pi]$. Thus, a second piece of information is obtained using

$$\cos\delta'' = \hat{\boldsymbol{V}}_\mathrm{ISSR} \cdot \hat{\boldsymbol{V}}_\mathrm{wind}. \tag{6}$$

With this, the final result is

$$
\begin{aligned}
\text{for} \quad \cos\delta'' > 0 \quad &: \quad \delta = \delta' \\
\text{for} \quad \cos\delta'' < 0 \quad \text{and} \quad \delta' < 0 \quad &: \quad \delta = -\pi - \delta' \\
\text{for} \quad \cos\delta'' < 0 \quad \text{and} \quad \delta' > 0 \quad &: \quad \delta = \pi - \delta'.
\end{aligned}
\tag{7}
$$

3.5 Rotation of ISSRs

As ISSRs are extended features, their characterisation with the COP is just the first of a series of conceivable moments. The second moments (inertia in the mechanical analogue) form a covariance matrix from which further characteristics can be derived via its eigenvalues and eigenvectors. The former can be used to compute an eccentricity of the ISSR, while the latter provide the principal axes of an ISSR.

For a given ISSR with N grid points the covariance matrix is

$$\Theta = \begin{pmatrix} \sum_{n=1}^{N} PPC_{\mathrm{prob}_n} \cdot (x_n - x_\mathrm{COP})^2 & \sum_{n=1}^{N} PPC_{\mathrm{prob}_n} \cdot (x_n - x_\mathrm{COP}) \cdot (y_n - y_\mathrm{COP}) \\ \sum_{n=1}^{N} PPC_{\mathrm{prob}_n} \cdot (x_n - x_\mathrm{COP}) \cdot (y_n - y_\mathrm{COP}) & \sum_{n=1}^{N} PPC_{\mathrm{prob}_n} \cdot (y_n - y_\mathrm{COP})^2 \end{pmatrix}. \tag{8}$$

As Θ is a symmetric matrix, it has real eigenvalues and the eigenvectors are orthogonal. The eigenvector corresponding to the larger eigenvalue, $\boldsymbol{V}_{\mathrm{PA}}$, defines the principal axis (PA) and the other one the minor axis (MA) of the ISSR. The angle, α, between the principal axis at t_{n-1} and t_{n+1} is determined with the same convention as the angle δ from above: If it needs a anticlockwise rotation to turn $\boldsymbol{V}_{\mathrm{PA}}(t_{n-1})$ onto $\boldsymbol{V}_{\mathrm{PA}}(t_{n+1})$, $\alpha > 0$, otherwise $\alpha \leq 0$. The calculation of α is thus analogue to the calculation of δ:

$$\alpha' = \arcsin\left(\langle \hat{\boldsymbol{V}}_{\mathrm{PA}}(t_{n-1}), \hat{\boldsymbol{V}}_{\mathrm{PA}}(t_{n+1}), \hat{\boldsymbol{z}}\rangle\right), \quad \cos\alpha'' = \hat{\boldsymbol{V}}_{\mathrm{PA}}(t_{n-1}) \cdot \hat{\boldsymbol{V}}_{\mathrm{PA}}(t_{n+1}), \tag{9}$$

and then the distinction of the cases (c.f. Equation 7) yields α.

α can be used to define a kind of angular velocity (pseudo-angular velocity) by dividing it by the temporal difference $t_{n+1} - t_{n-1}$:

$$\dot{\alpha} = \frac{\alpha}{t_{n+1} - t_{n-1}}. \tag{10}$$

Angular velocities are features of extended objects and thus not comparable to either the veering of the wind or its rotation, which are local quantities.

3.6 An example

An illustration of the methods and how they work is given in figures 1 and 2. The map of Figure 1 shows the domain of the ICON-EU model. The coloured areas are CISSRs ($PPC = 1$) that are sufficiently large according to the conditions set out above. The different colours mark different individuals that should be identified in the same forecast run one hour earlier and later. An identification in further forecast hours or even in forecasts with different initialisation times may be tried as well for the purpose of forecast verification. This has been done for the D-KULT project, but is not in the scope of the present paper.

The characterisation of an individual CISSR is exemplified in Figure 2. The coloured area again marks an individual CISSR. Its COP is located at the intersection of the coloured straight lines. Note that the COP lies not necessarily within the CISSR if the latter has a strongly bent shape. The red-orange lines are the major principal and the yellow ones the minor principle axes of the CISSRs.
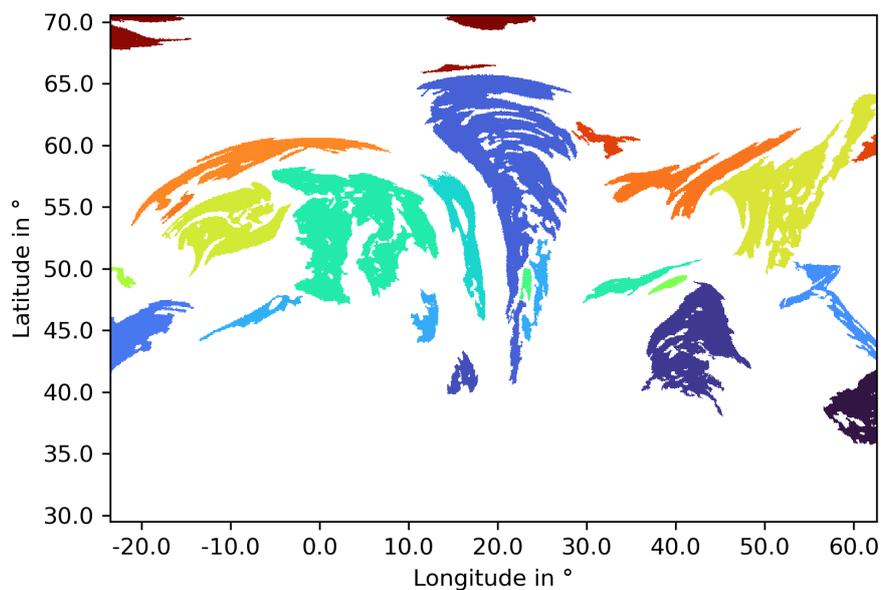
Figure 1. Map of the area covered by ICON-EU with regions where $PPC = 1$ (CISSRs) marked in different colours for the example situation from 04.04.2024 at 12 UTC initialisation for $+15$ hours at approximately $301\,\mathrm{hPa}$. These individual CISSRs may be identified in earlier and later forecast hours and in forecasts with differing initialisation time using the methods described in the text.

(a) Situation at t_{n-1}. (b) Situation at t_n. (c) Situation at t_{n+1}.
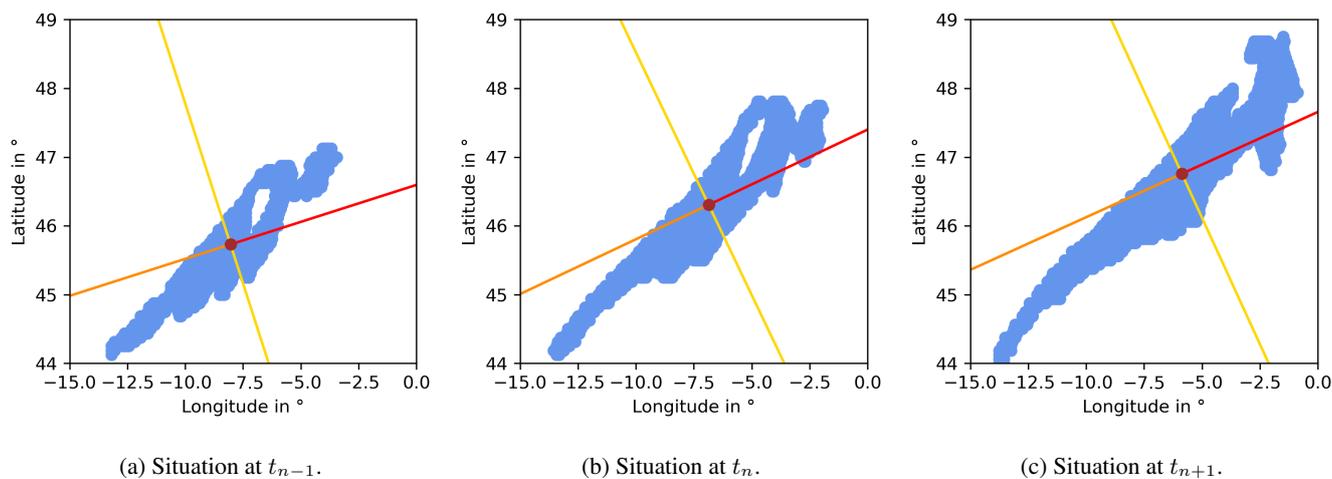
Figure 2. Basic characteristics of individual CISSRs: The CISSR, that is the grid points with $PPC = 1$ is marked in blue for t_{n-1} (Figure 2a), for t_n (Figure 2b), and for t_{n+1} (Figure 2c). The centre of the crossed lines is the centre of probability (COP). The red-orange lines are the major principal and the yellow ones the minor principle axes of the CISSRs. Note: The CISSR in Figure 2b corresponds to the light blue CISSR in Figure 1 in the southwest between approximately $-15°$ to $0°$ longitude and $44°$ to $49°$ latitude.

4 Results

4.1 The relative motion of air and embedded ISSRs

4.1.1 Speeds

Figure 3 (left) shows the histogram of pseudo-velocities of ISSRs calculated according to Equation 2. The distribution of ISSR velocities has a mean and a standard deviation of $15.5\,\mathrm{m\,s^{-1}}$ (black line) and $9.7\,\mathrm{m\,s^{-1}}$ (blue lines). The median is $13.7\,\mathrm{m\,s^{-1}}$ (red line). The distribution is right skewed with a skewness of about 1.1. The corresponding distribution for the wind speeds at the COPs of the ISSRs, calculated according to Equation 4, are shown in Figure 3 (right). The distribution of wind velocities has a mean and a standard deviation of $21.4\,\mathrm{m\,s^{-1}}$ (black line) and $11.5\,\mathrm{m\,s^{-1}}$ (blue lines). The median is $20.0\,\mathrm{m\,s^{-1}}$ (red line). The distribution is right skewed with a skewness of about 0.7. Both distributions can be well approximated by a Weibull distribution (orange), a generalised exponential distribution, which is defined as follows:

$$f(v) = \gamma \cdot m \cdot v^{(m-1)} \cdot \exp\left(-\gamma \cdot v^m\right). \tag{11}$$

The two parameters m and γ can be determined by plotting the cumulative distribution functions (CDF) of the pseudo-velocities of ISSRs V_{ISSR} and the wind speeds V_{wind} on a so-called Weibull paper (Gierens and Brinkop, 2002), where the x-axis is $\log v$ and the y-axis is $\log(\log(1/(1 - CDF)))$. For an illustration see Figure C1 in Appendix C. In this representation, the two CDFs can be approximated by straight lines, which indicates that the original distributions can be approximated very well by Weibull distributions. The slopes are $m_{\mathrm{ISSR}} = 1.85$ and $m_{\mathrm{wind}} = 1.9$. The intercepts (s) are related to $\gamma = e^s$. These intercepts are $s_{\mathrm{ISSR}} = -5.2$ and $s_{\mathrm{wind}} = -6$, which are obtained by fitting the two lines to the CDFs in the Weibull paper. Wind data have been fitted by Weibull distributions already by Dixon and Swift (1984).
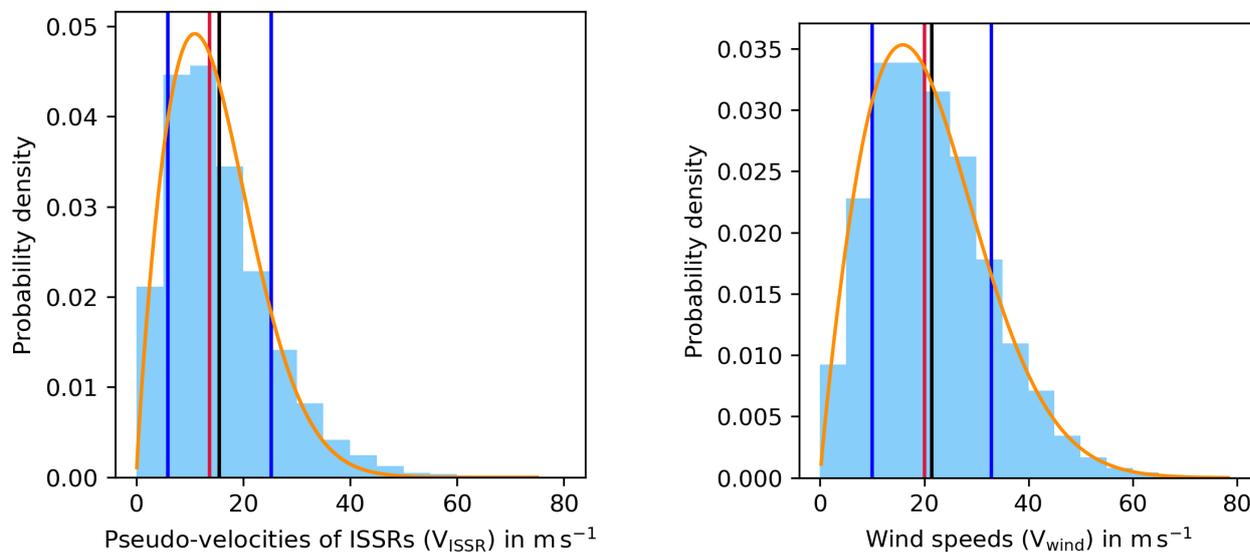
Figure 3. Histograms of pseudo-velocities of ISSRs (left) and wind speeds (right) in $\mathrm{m\,s^{-1}}$. The histograms are normalised such that they present approximations of probability density functions, with a resolution of $5\,\mathrm{m\,s^{-1}}$. Means (black) $\pm$ standard deviations (blue) as well as the medians (red) are indicated. The orange curves show Weibull distributions that fit the left histogram quite well and the right one excellently. Please note the different scales on the y-axes in both panels.

The distribution of individual differences of pseudo-velocities of ISSRs and of the real wind speeds at ISSR COPs is nearly symmetric (the skewness is almost zero, -0.1) with a peak around $0\,\mathrm{m\,s^{-1}}$, see Figure 4. This means that the velocities of ISSRs and the wind in the COP hardly differ in most cases. The mean of the distribution is $-5.9\,\mathrm{m\,s^{-1}}$ (black) and the standard deviation is $12.8\,\mathrm{m\,s^{-1}}$ (blue). The median of this distribution is $-5.3\,\mathrm{m\,s^{-1}}$ (red). As expected for a peaked distribution, 190 the kurtosis (1.57) exceeds zero significantly, if we estimate its uncertainty with $\delta(\mathrm{kurtosis}) \approx \sqrt{(24/N)} \approx 0.03$, where $N = 29595$ is the number of data in the histogram (Press et al., 1989, p. 457). In rare cases the speed differences exceed $50\,\mathrm{m\,s^{-1}}$ in both directions.
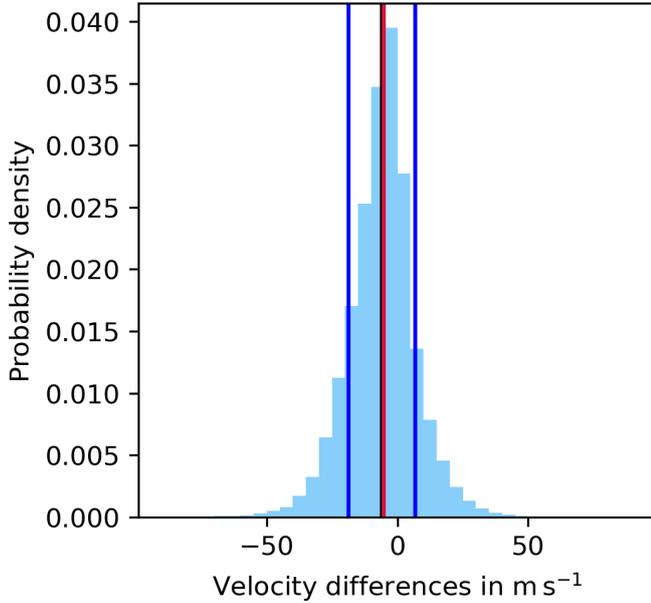
Figure 4. Histogram of velocity differences: pseudo-velocities of ISSRs minus the wind speeds in $\mathrm{m\,s^{-1}}$. The histogram is normalised, such that it represents an approximation of the corresponding probability density, with a resolution of $5\,\mathrm{m\,s^{-1}}$. The mean (black) $\pm$ one standard deviation (blue) are indicated as well as the median (red).

Figure 5 shows a joint histogram for ISSR pseudo-speeds and wind speeds. The highest density of cases is at low pseudo-velocities of ISSRs with slightly higher wind speeds. In order to see whether the two (marginal) distributions of the pseudo-velocities of ISSRs and of the wind speeds differ significantly, we perform a Kolmogorov-Smirnov test on the pair of their corresponding cumulative distribution functions, see Figure 6. To do this, we test the null hypothesis H_0 that $F_{V_{\mathrm{ISSR}}} = F_{V_{\mathrm{wind}}}$, which states that the two distributions are equal. The alternative hypothesis H_1 is $F_{V_{\mathrm{ISSR}}} \neq F_{V_{\mathrm{wind}}}$ i.e. that the two distribution functions do not match. We select a significance level $\alpha = 5\%$. If H_0 is rejected on this level, H_1 can be accepted and the likelihood that this result is wrongly obtained by chance is less than 5%. For the test, the maximum vertical distance D between the two CDFs ($F_{V_{\mathrm{ISSR}}}$ and $F_{V_{\mathrm{wind}}}$) is determined. The larger this distance, the more likely H_0 is rejected. The test statistic D and the p-value are calculated using the statistics software package R, which yields $D \approx 0.19$ and $p < 2.2 \cdot 10^{-16}$. This p-value is so much smaller than the significance level, that the exact choice of α does not matter: The null hypothesis H_0 can firmly be rejected and the two distributions, $F_{V_{\mathrm{ISSR}}}$ and $F_{V_{\mathrm{wind}}}$, differ significantly from each other. That is, the differences may be small, but they are real.

Finally, we study the (linear) correlation between the ISSR speeds and the wind speeds. It measures how the individual ISSR speeds deviate from their mean in a positive or negative direction when simultaneously the wind speeds deviate positively or negatively from their mean and vice versa. This quantity is given as

$$\mathrm{Corr}(V_{\mathrm{ISSR}}, V_{\mathrm{wind}}) = \frac{1}{\sigma_{V_{\mathrm{ISSR}}} \sigma_{V_{\mathrm{wind}}}} \sum_i (V_{\mathrm{ISSR},i} - \langle V_{\mathrm{ISSR}} \rangle)(V_{\mathrm{wind},i} - \langle V_{\mathrm{wind}} \rangle), \tag{12}$$

where the σ_x are the two standard deviations and the means are indicated with angular brackets. The sum extends over all our cases. We find a quite moderate correlation of 0.28 for the two speed values. This might seem surprising since the absolute speed differences are mainly small. But it simply indicates that the speed differences are positive and negative with similar probability.
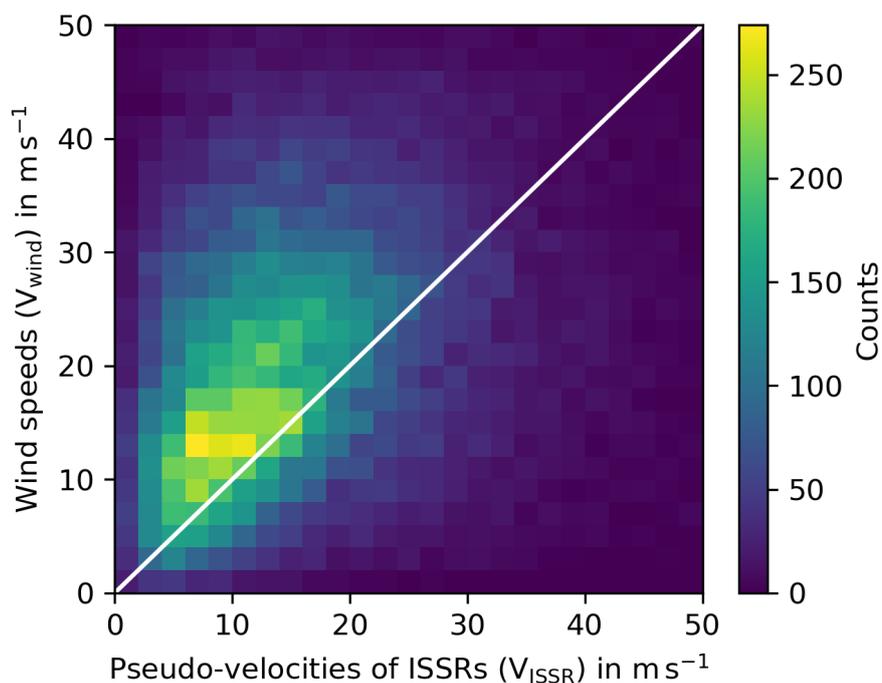
Figure 5. Joint histogram of ISSR pseudo-wind speeds and real air wind speeds at the position of the ISSR COPs. The number of joint occurrences in $2\,\mathrm{m\,s^{-1}} \times 2\,\mathrm{m\,s^{-1}}$ square bins are given in the colour bar. The white diagonal marks the points where the two speeds are equal (or nearly so). Higher speeds than $50\,\mathrm{m\,s^{-1}}$ occur in our data, but very rarely.
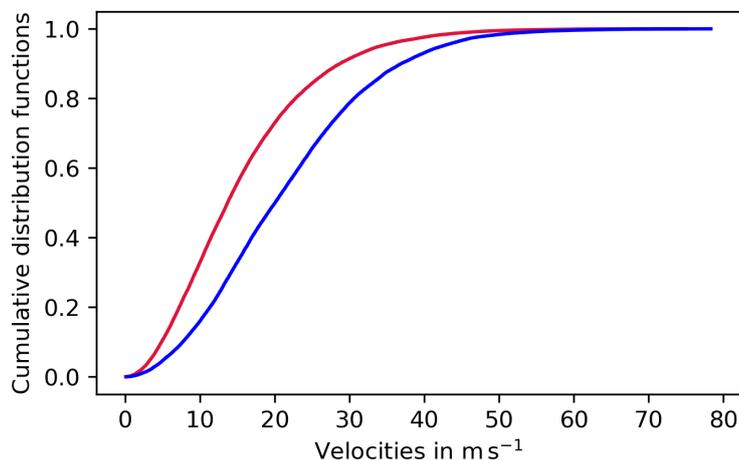
Figure 6. Cumulative distribution functions $F_{V_{\mathrm{ISSR}}}$ (red) and $F_{V_{\mathrm{wind}}}$ (blue) .

4.1.2 Directions

Next, we consider the direction of the movement of the ISSRs and the wind at their COPs separately, where $0°$ refers to
215 movement to the north and $90°$ corresponds to eastward motion, see Figure 7. Both histograms show that the most frequent
direction of motion of ISSRs and of the winds at ISSR COPs is eastward. There is also a second maximum in the westward
direction for the direction of ISSR movements, but this is much weaker than the eastward maximum. The similarity of the
histograms does not necessarily imply that the motion of an ISSR and the wind at its COP are often aligned as the histograms
show the statistics of both quantities separately. To check this, we consider again a two-dimensional histogram, that is, the
220 joint probability of the directions of motion (Figure 8). This shows that both ISSRs and the wind usually move in very similar
directions, that is, the motions are aligned.
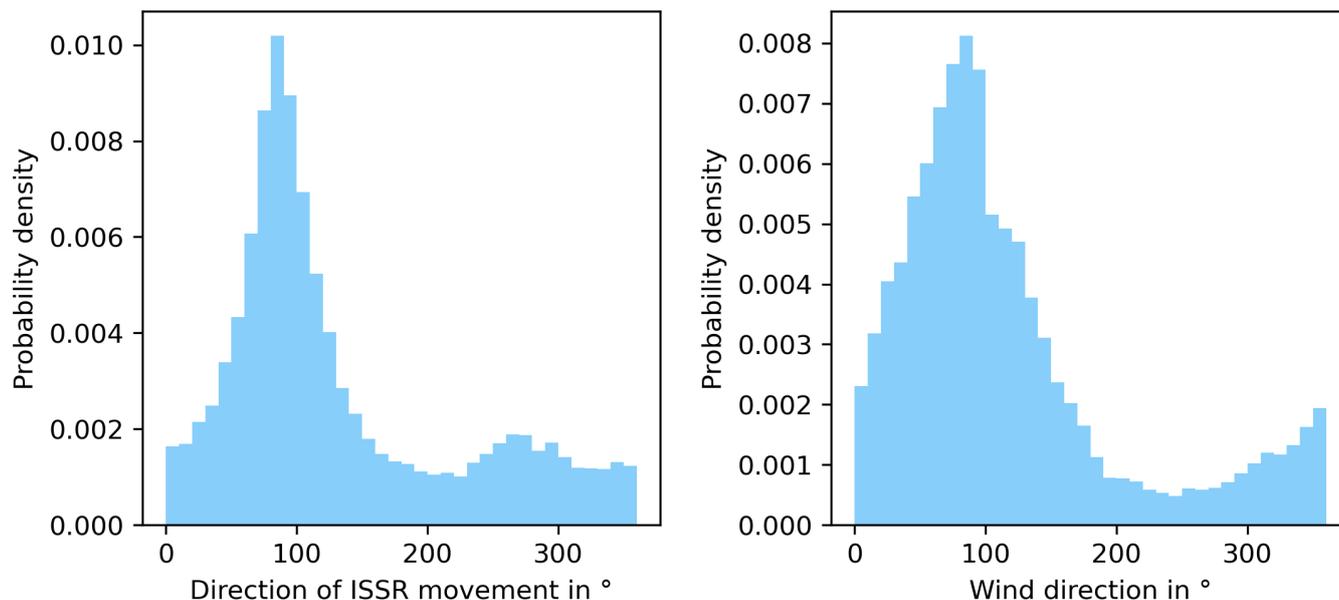
Figure 7. Histograms of the direction of movement of ISSRs (left panel) and the wind at their COPs (right panel). Angles range from 0° to 360°, where 0° or 360° means movement to the north, 90° a movement to the east, and so on. The histograms are normalised, such that they represent approximations of the corresponding probability densities, with a resolution of 10°. The histograms are very similar. Both have their maximum between 80° and 90° degrees, which indicates a predominant west-to-east movement.

Figure 9 shows the differences of both directions of motion. In this histogram, positive angles mean that the wind vector is in counterclockwise direction from the pseudo-wind vector (e.g. the ISSR moves eastward while the air moves to the north). The mean angle is 2.3° with a standard deviation of 65.2°. The median is 1.1°. If their directions differ then the difference is
225 slightly more common in the anti-clockwise direction than in the clockwise direction, see Figure 8.
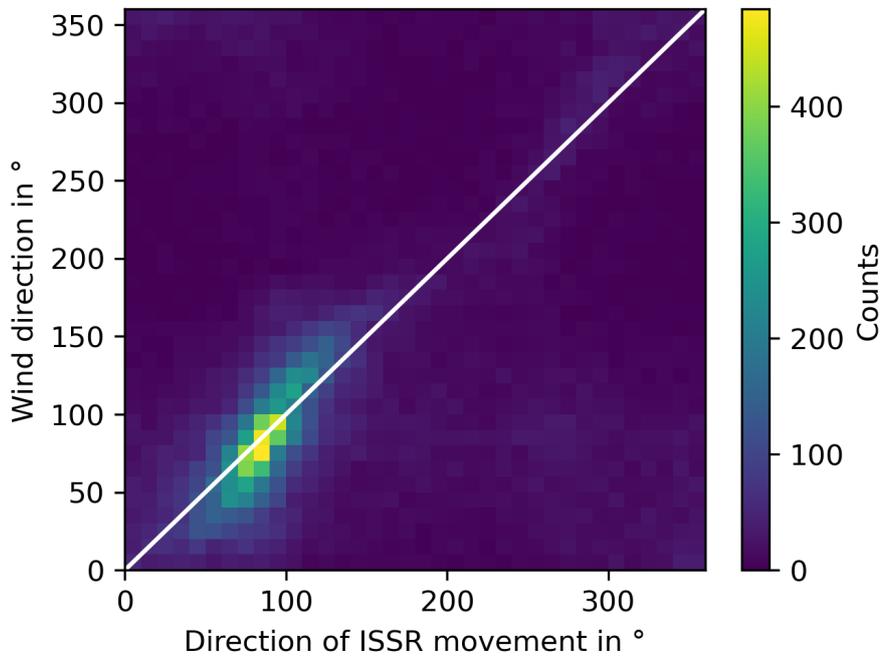
Figure 8. Joint probability distribution of the direction of motion of ISSRs and the wind at their COPs. The number of joint occurrences in $10° \times 10°$ square bins are given in the colour bar. The white diagonal marks the points where the two directions are equal (or nearly so). The alignment is quite strong.
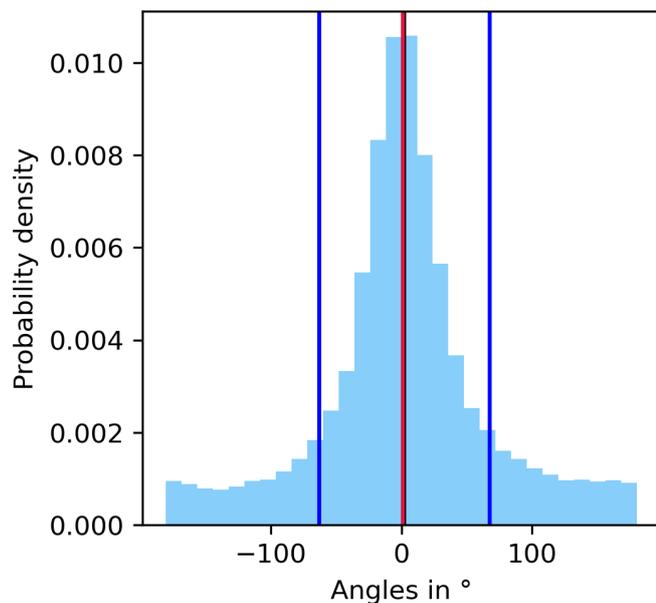
Figure 9. Histogram of the angles (in degree) between the movement of ISSRs (vector of COP at t_{n-1} and COP at t_{n+1}) and wind vectors from $-180°$ to $180°$. Positive angles mean counterclockwise rotation from the ISSR vector to the wind vector. The histogram is normalised, such that it represents an approximation to a probability density function, with a resolution of $12°$. Mean $\pm$ one standard deviation are indicated with the black and blue lines and the median with a red line, respectively.

4.2 Rotation of ISSRs

The rotation of ISSRs is treated, as stated above, as the rotation of its principle axes in time. This can be caused by a real rotation (if the whole system rotates), but a change of the shape or the spatial distribution of probability around the COP can induce rotation of the principle axes as well; thus it is appropriate to speak of a pseudo-rotation with a corresponding pseudo-angular
230 speed.

Figure 10 shows a histogram of the pseudo-angular speed of ISSRs. It is remarkably symmetric around zero (the skewness is almost zero) and peaks at zero. That is, ISSRs most often do hardly rotate and if so, they do it with similar probability in clockwise and anti-clockwise directions. Accordingly, both mean and median are very nearly $0° \, \text{h}^{-1}$ (black and red line) with a standard deviation of $27.9° \, \text{h}^{-1}$ (blue lines).
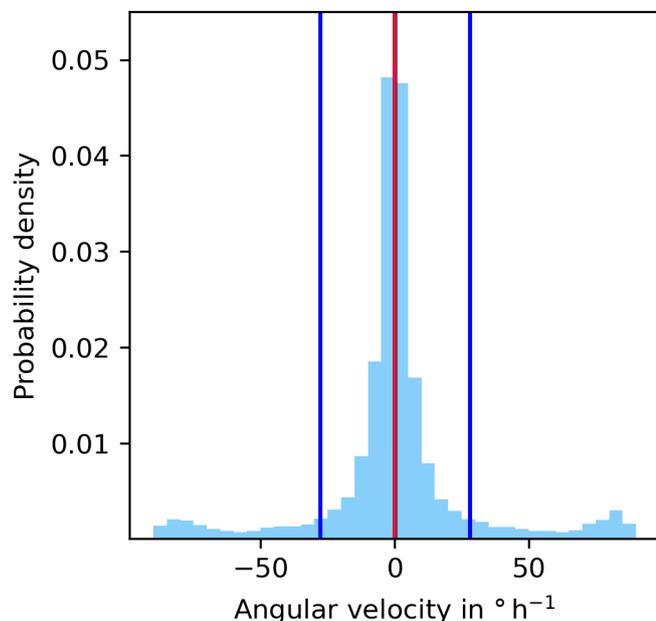
Figure 10. Histogram of the differences in angles between the principal axis of t_{n-1} and principal axis of t_{n+1} covered within two hours, i.e. the angular velocity $\dot{\alpha}$ (in $^\circ\,\mathrm{h}^{-1}$). The histogram is normalised, such that it represents an approximation of the corresponding probability density, with a resolution of $5^\circ\,\mathrm{h}^{-1}$. The mean (black) $\pm$ one standard deviation (blue) are indicated as well as the median (red). Note, that the median and the mean are nearly the same. For this reason the former one can hardly be seen.

5 Discussion

5.1 Discussion of the methods

This analysis was constrained to horizontal movement only, for the sake of simplicity. This means that the vertical movement of ISSRs was not taken into account. This might seem surprising since vertical lift of moist air is the primary source of ice supersaturation (Gierens et al., 2012). However, vertical movements are two to three orders of magnitudes smaller than horizontal movements in the atmosphere. Therefore we think that this simplification may be justified. Anyway, vertical movements of ISSRs could pretend horizontal movements (e.g. by shape changes) or could perturb the identification of ISSRs in consecutive forecasts. In addition, one ISSR can suddenly disappear (within one hour) and another one can appear in that vicinity, so that this one is interpreted as the actual ISSR. Two ISSRs can also coagulate to a single one or vice versa. In principle, the mechanistic parts of this study (i.e., determination of the COP and the principle axes) can be performed in three dimensions straightforwardly, but the problems with the identification of ISSRs in consecutive forecasts would become much more involved. For instants, application of the Hu moments would not be possible. Therefore, this study constrains the analysis to two dimensions.

ISSRs are not rigid bodies, they generally change shape, extension and total probability while they move and rotate. Thus, one could think of dividing their kinematic properties into internal and external effects, internal being the change in shape and
250 total probability, and external the "true" shift and rotation. Both, internal and external effects change the COP and the principle axes, but it is very difficult and perhaps even impossible or useless to disentangle internal and external effects. One could argue that external effects are caused by shifts and rotation of the material system (the air) that contains the ISSR, that is, it would be characterised by V_{wind} and a large-scale rotation of the air. Then the difference $V_{\mathrm{ISSR}} - V_{\mathrm{wind}}$ would be completely due to internal changes of shape, extension and probability distribution of an ISSR. But, a similar case, that of a foehn cloud, where
255 the wind blows into and out of it while the cloud is stationary, shows, that this interpretation is strange. It would imply that the foehn cloud would move with the wind proper, but then internal changes would completely drive it back.

Considering rotation, the situation is analogous, but also numerically quite difficult. A large scale rotation of the air could be given by the circulation of the wind along the perimeter of an ISSR which, however, is not well defined in a discrete model space. Similarly, the partition of rotation of the ISSR into external and internal cannot be computed adequately since rotation
260 is not well defined in discrete spaces (e.g. Thibault, 2010). Because of these unsolved problems, we have not tried to separate V_{ISSR} or $\dot{\alpha}$ into external and internal contributions.

We admit that the study is based on only two months of data and it is confined to the EU-nest of the ICON model. As the atmospheric dynamics which is at the base of our findings changes seasonally and geographically, the relation between ISSR motion and the motion of the ambient wind may change from season to season and geographically, in particular in the
265 meridional direction. However, the data necessary to check this become available only in the coming months in the course of the project.

5.2 Implications for contrail lifetimes

It turned out that ISSRs move very often with similar speeds and in similar directions as the wind at their COPs do. A similar direction of the movements implies that contrails are not easily blown out of their ambient ISSRs which favours the growth
270 of their ice crystals. In such cases contrails end once their crystals are sufficiently large for sedimentation or once the ice supersaturation itself vanishes by subsidence, increasing temperature and thus decreasing relative humidity. However, contrail lifetimes are not controlled by the lifetime of their parent ISSR for the rare cases where wind and ISSR directions differ. In such cases contrails are blown out of the ISSR with the wind. The reverse process is not possible; persistent contrails cannot be blown into an ISSR because if a contrail does not form within an ISSR, it evaporates quickly so there is nothing left to be blown
275 into the ISSR. Thus, individual contrails must have a shorter lifetime on average than their parental ISSR exists. However, an ISSR may be always filled with new contrails if new aircraft cross it producing new contrails. This has been observed 30 years ago by Bakan et al. (1994).

5.3 Application to other features

The presented method has originally been developed for verification of forecasts of CISSRs. An older forecast is to be com-
280 pared to a newer forecast for the same valid time. The latter forecast serves as a proxy for the reality that is not otherwise

available. With the mechanical method we simply determine the COPs and principle axes of individual CISSRs in both forecasts, additionally to their size and total probability, and calculate the individual differences (or other statistics if desired). We note that the method can be used for other features as well, for instance for areas where aircraft non-CO_2 emissions would have a particularly large climate effect. For this purpose, we would use the (algorithmic) Climate Change function fields (Dietmüller et al., 2022; Yin et al., 2023), select a threshold (which isolates maxima) and use the value of the aCCF (or the excess over the threshold) in place of the PPC_{prob}. Then everything else is completely analogous to the analyses presented in the current paper.

6 Conclusion

In this study, two months of WAWFOR data of DWD are analysed to obtain information about the movement of ice supersaturated regions (ISSRs) and to compare this with the local wind at the ISSRs. To this end we use humidity, temperature and wind information and determine the location of ISSRs. We develop a procedure to identify ISSRs in three consecutive forecasts. For each ISSR we determine a centre of probability (COP) and the principle axes at this point. Speeds of ISSRs are determined by the movement of the COPs together with rotations of their principle axes. For these positions the wind speeds and the rotation of the wind vectors are recorded. These data form the basis of our comparisons.

On average, the wind speeds are larger than the ISSR movement speed. The mean of the Pseudo-velocities of ISSRs is approximately $16\,\text{m}\,\text{s}^{-1}$. The mean of the wind speeds is around $21\,\text{m}\,\text{s}^{-1}$. Both distributions, the ISSR speed and the wind speed, follow a Weibull distribution very well. In most cases ISSRs move at a similar speed as the local wind. An analogous statement pertains to the directions of the movement. Both ISSRs and the local wind move in most cases in eastward direction. Extended ISSRs not only move straight forward but also rotate, but quite slowly. Within one hour the rotation angle rarely exceeds $\pm 10°$. Clockwise and counterclockwise rotations occur with almost equal probability.

The study results imply that persistent contrails, which move with the wind, should often move parallel to and inside their parent ISSR. Under this condition, the lifetime of contrails is constrained by sedimentation of ice crystals or by the end of the lifetime of the ISSR itself. Once ISSRs and the wind move in different directions, contrails are blown out of the ISSR into the subsaturated environment and vanish.

Finally we note, that the methods used in this paper can be applied to other extended features in the atmosphere in an analogous way, for instance for the purpose of forecast verification.

Code availability. Python codes can be shared on request.

Data availability.

Appendix A: Hu-moments

310 Hu-moments are based on normalised central moments. The general formula of normalised central moments in our application is:

$$\eta_{k,l} = \frac{\sum_x \sum_y PPC_{\text{prob}}(x,y) \cdot (x - x_{\text{COP}})^k \cdot (y - y_{\text{COP}})^l}{[\sum_x \sum_y PPC_{\text{prob}}(x,y)]^{1+\frac{k+l}{2}}}. \tag{A1}$$

All $\eta_{k,l}$ whose $k + l = 2$ are related to the entries of the covariance matrix Θ (see Equation 8).

Normalised central moments are invariant to translation and scale. The advantage of the seven Hu-moments is that they are
315 invariant to translation, scale and rotation. The first six Hu-moments are also invariant to reflection; however, for the seventh
Hu-moment the sign changes for reflection. The Hu-moments can be calculated this way (Prokop and Reeves, 1992; Huang
and Leng, 2010; Mallick and Bapat, 2018):

$$
\begin{align}
h_1 &= \eta_{20} + \eta_{02} \tag{A2}\\
h_2 &= (\eta_{20} - \eta_{02})^2 + 4 \cdot \eta_{11}^2 \tag{A3}\\
320 \quad h_3 &= (\eta_{30} - 3 \cdot \eta_{12})^2 + (3 \cdot \eta_{21} - \eta_{03}^2) \tag{A4}\\
h_4 &= (\eta_{30} + \eta_{12})^2 + (\eta_{21} + \eta_{03})^2 \tag{A5}\\
h_5 &= (\eta_{30} - 3 \cdot \eta_{12}) \cdot (\eta_{30} + \eta_{12}) \cdot [(\eta_{30} + \eta_{12})^2 - 3 \cdot (\eta_{21} + \eta_{03})^2] + \tag{A6}\\
&\quad + (3 \cdot \eta_{21} - \eta_{03}) \cdot (\eta_{21} + \eta_{03}) \cdot [3 \cdot (\eta_{30} + \eta_{12})^2 - (\eta_{21} + \eta_{03})^2] \tag{A7}\\
h_6 &= (\eta_{20} - \eta_{02}) \cdot [(\eta_{30} + \eta_{12})^2 - (\eta_{21} + \eta_{03})^2 + 4 \cdot \eta_{11} \cdot (\eta_{30} + \eta_{12}) \cdot (\eta_{21} + \eta_{03})]) \tag{A8}\\
325 \quad h_7 &= (3 \cdot \eta_{21} - \eta_{03}) \cdot (\eta_{30} + \eta_{12}) \cdot [(\eta_{30} + \eta_{12})^2 - 3 \cdot (\eta_{21} + \eta_{03})^2] + \tag{A9}\\
&\quad + (\eta_{30} - 3 \cdot \eta_{12}) \cdot (\eta_{21} + \eta_{03}) \cdot [3 \cdot (\eta_{30} + \eta_{12})^2 - (\eta_{21} + \eta_{03})^2]. \tag{A10}
\end{align}
$$

Since the seven Hu-moments have different orders of magnitude and are therefore difficult to compare, they are adjusted using
a log transformation:

$$H_i = -\text{sgn}(h_i) \cdot \log(|h_i|). \tag{A11}$$

330 These log transformed H_i are then combined and a difference can be calculated that reflects the similarity difference between
two forms of ISSR A and ISSR B:

$$D(A,B) = \sum_{i=1}^{7} \left| \frac{1}{H_i^B} - \frac{1}{H_i^A} \right|. \tag{A12}$$

In order to identify two shapes of ISSR A and ISSR B in subsequent forecasts, $D(A,B)$ should be as small as possible.

Appendix B: Distances on great circles

335 The distance between two points with longitudes $\lambda_{1,2}$ and latitudes $\varphi_{1,2}$ on a sphere can be determined using the equations
for an orthodrome, i.e. the shortest connection between two points on a sphere (see any textbook on navigation or spherical
geometry and trigonometry). Let us assume that $\lambda_{1,2}$ and $\varphi_{1,2}$ are given in radians. Let $\Delta_\lambda = |\lambda_1 - \lambda_2|$. Then the distance,
$d_{1,2}$, on the surface of the Earth is given as.

$$d_{1,2} = R \arccos\left[\sin(\varphi_1)\sin(\varphi_2) + \cos(\varphi_1)\cos(\varphi_2) \cdot \cos(\Delta_\lambda)\right], \tag{B1}$$

340 with the radius of the Earth $R \approx 6373\,\text{km}$. In case, that the longitudes and latitudes are given in degrees, they must be translated
into radians with the factor $\pi/180°$.

Appendix C: Cumulative distribution functions of the pseudo-velocities of ISSRs and the wind speeds plotted on Weibull paper
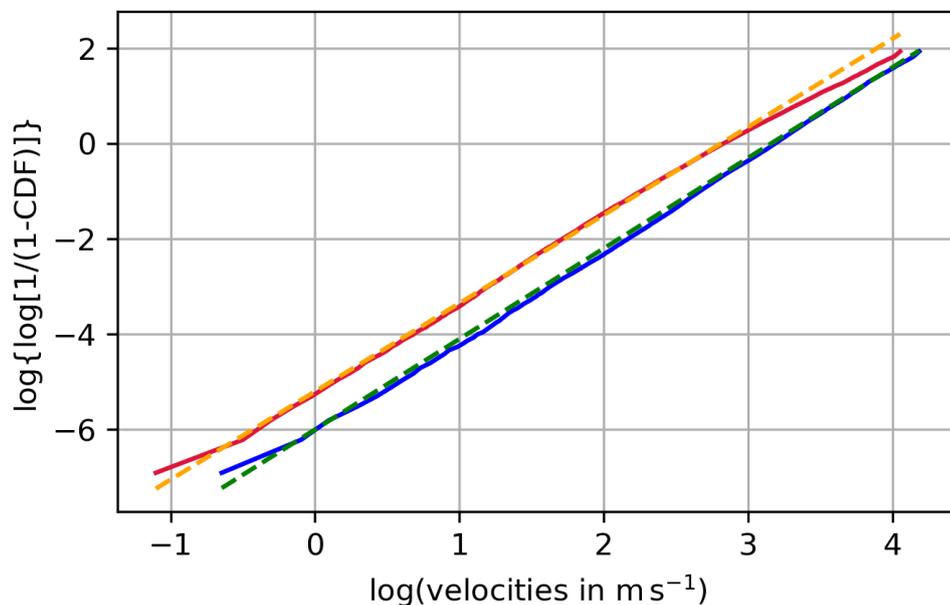
Figure C1. Cumulative distribution functions of the pseudo-velocities of ISSRs V_{ISSR} (red) and the wind speeds V_{wind} (blue) plotted on
Weibull paper together with linear fits as dashed lines: $g_{\text{ISSR}} = 1.85 \cdot x - 5.2$ (orange) and $g_{\text{wind}} = 1.9 \cdot x - 6$ (green).

Author contributions. This paper is part of SH's PhD thesis. SH wrote the codes, ran the calculations, analysed the results and produced the
345 figures. KG supervises her research. Both authors discussed the methods and results and wrote the paper.

Competing interests. The authors declare no competing interests.

Acknowledgements. This research contributes to and is supported by the project D-KULT, Demonstrator Klimafreundliche Luftfahrt (Förderkennzeichen 20M2111A), within the Luftfahrtforschungsprogramm LuFo VI of the German Bundesministerium für Wirtschaft und Klimaschutz. This work used resources of the Deutsches Klimarechenzentrum (DKRZ) granted by its Scientific Steering Committee (WLA) under project

350   ID bd1357. The authors would like to thank Annemarie Lottermoser for her thorough reading and commenting a draft manuscript.

References

Bakan, S., Betancor, M., Gayler, V., and l, H. G.: Contrail frequency over Europe from NOAA–satellite images, Ann. Geophys., 12, 962–968, 1994.

Dietmüller, S., Matthes, S., Dahlmann, K., Yamashita, H., Simorgh, A., Soler, M., Linke, F., Lührs, B., Meuser, M., Weder, C., Grewe, V., Yin, F., and Castino, F.: A python library for computing individual and merged non-CO2 algorithmic climate change functions: CLIMaCCF V1.0, Geosci. Model Dev. Discuss., under review, https://doi.org/10.5194/gmd-2022-203, 2022.

Dixon, J. and Swift, R.: The directional variation of wind probability and Weibull speed parameters, Atmospheric Environment (1967), 18, 2041–2047, https://doi.org/https://doi.org/10.1016/0004-6981(84)90190-2, 1984.

Dutton, J.: The Ceaseless Wind: An Introduction to the Theory of Atmospheric Motion, Dover books on earth sciences, Dover Publications, https://books.google.de/books?id=g7URAQAAIAAJ, 1986.

Gierens, K. and Brinkop, S.: A model for the horizontal exchange between ice–supersaturated regions and their surrounding area, Theor. Appl. Climatol., 71, 129–140, 2002.

Gierens, K. and Brinkop, S.: Dynamical characteristics of ice supersaturated regions, Atmos. Chem. Phys., 12, 11 933 –11 942, 2012.

Gierens, K., Spichtinger, P., and Schumann, U.: Ice supersaturation, in: Atmospheric Physics. Background — Methods — Trends, edited by Schumann, U., chap. 9, pp. 135–150, Springer, Heidelberg, Germany, 2012.

Gierens, K., Wilhelm, L., Hofer, S., and Rohs, S.: The effect of ice supersaturation and thin cirrus on lapse rates in the upper troposphere, Atmos. Chem. Phys., 22, 7699–7712, https://doi.org/10.5194/acp-22-7699-2022, 2022.

Grewe, V., Gangoli, A. R., Gronstedt, T., Xisto, C., Linke, F., Melkert, J., Middel, J., Ohlenforst, B., Blakey, S., Christie, S., Matthes, S., and Dahlmann, K.: Evaluating the climate impact of aviation emission scenarios towards the Paris agreement including COVID-19 effects, Nature Communications, 12:3841, 1–10, https://doi.org/10.1038/s41467-021-24091-y, 2021.

Hofer, S., Gierens, K., and Rohs, S.: How well can persistent contrails be predicted? — An update, Atmos. Chem. Phys., 24, 7911—-7925, https://doi.org/10.5194/acp-24-7911-2024, 2024.

Huang, Z. and Leng, J.: Analysis of Hu's moment invariants on image scaling and rotation, in: 2010 2nd International Conference on Computer Engineering and Technology, vol. 7, pp. V7–476–V7–480, 2010.

Irvine, E. and Shine, K.: Ice supersaturation and the potential for contrail formation in a changing climate, Earth Syst. Dynam., 6, 555–568, https://doi.org/10.5194/esd-6-555-2015, 2015.

Lee, D., Fahey, D., Skowron, A., Allen, M., Burkhardt, U., Chen, Q., Doherty, S., Freeman, S., Forster, P., Fuglestvedt, J., Gettelman, A., De León, R., Lim, L., Lund, M., Millar, R., Owen, B., Penner, J., Pitari, G., Prather, M., Sausen, R., and Wilcox, L.: The contribution of global aviation to anthropogenic climate forcing for 2000 to 2018, Atmos. Env., 244, 117 834, https://doi.org/10.1016/j.atmosenv.2020.117834, 2021.

Mallick, S. and Bapat, K.: Shape Matching using Hu Moments (C++/Python), LearnOpenCV, last access April 2024, https://learnopencv.com/shape-matching-using-hu-moments-c-python/, 2018.

Matthes, S., Lim, L., Burkhardt, U., Dahlmann, K., Dietmüller, S., Grewe, V., Haslerud, A. S., Hendricks, J., Owen, B., Pitari, G., Righi, M., and Skowron, A.: Mitigation of Non-CO2 Aviation's Climate Impact by Changing Cruise Altitudes, Aerospace, 8, 1–20, https://doi.org/10.3390/aerospace8020036, 2021.

Petzold, A., Neis, P., Rütimann, M., Rohs, S., Berkes, F., Smit, H., Krämer, M., Spelten, N., Spichtinger, P., Nedelec, P., and Wahner, A.: Ice-supersaturated air masses in the northern mid-latitudes from regular in situ observations by passenger aircraft: vertical distribution, seasonality and tropospheric fingerprint, Atmos. Chem. Phys., 20, 8157–8179, https://doi.org/10.5194/acp-20-8157-2020, 2020.

Press, W., Flannery, B., Teukolsky, S., and Vetterling, W.: Numerical recipes, Cambridge University Press, 1989.

390   Prokop, R. and Reeves, A.: A survey of moment-based techniques for unoccluded object representation and recognition, CVGIP: Graphical Models and Image Processing, 54, 438–460, https://doi.org/https://doi.org/10.1016/1049-9652(92)90027-U, 1992.

Schumann, U.: On conditions for contrail formation from aircraft exhausts, Meteorol. Z., 5, 4–23, 1996.

Spichtinger, P., Gierens, K., Leiterer, U., and Dier, H.: Ice supersaturation in the tropopause region over Lindenberg, Germany, Meteorol. Z., 12, 143–156, 2003.

395   Thibault, Y.: Rotations in 2D and 3D discrete spaces, Ph.D. thesis, Université Paris-Est, 2010.

Wolf, K., Bellouin, N., and Boucher, O.: Long-term upper-troposphere climatology of potential contrail occurrence over the Paris area derived from radiosonde observations, Atmos. Chem. Phys., 23, 287–309, https://doi.org/10.5194/acp-23-287-2023, 2023.

Yin, F., Grewe, V., Castino, F., Rao, P., Matthes, S., Dahlmann, K., Dietmüller, S., Frömming, C., Yamashita, H., Peter, P., Klingaman, E., Shine, K. P., Lührs, B., and Linke, F.: Predicting the climate impact of aviation for en-route emissions: The algorithmic climate change
400   function submodel ACCF 1.0 of EMAC 2.53, Geosci. Model. Dev., 16, 3313–3334, https://doi.org/10.5194/gmd-16-3313-2023, 2023.

Zängl, G., Reinert, D., Ripodas, P., and Baldauf, M.: The ICON (ICOsahedral Non-hydrostatic) modelling framework of DWD and MPI-M: Description of the non-hydrostatic dynamical core, QJRMS, 141, 563–579, https://doi.org/10.1002/qj.2378, 2015.